

Article

tRNA Fusion to Streamline RNA Structure Determination: Case Studies in Probing Aminoacyl-tRNA Sensing Mechanisms by the T-Box Riboswitch

Jason C. Grigg ^{1,2}, Ian R. Price ^{1,3} and Ailong Ke ^{1,*} 

¹ Department of Molecular Biology and Genetics, Cornell University, Ithaca, NY 14850, USA; griggj@mail.ubc.ca (J.C.G.); irp8@cornell.edu (I.R.P.)

² Department of Microbiology and Immunology, University of British Columbia, Vancouver, BC V6T1Z3, Canada

³ Department of Chemistry and Chemical Biology, Cornell University, Ithaca, NY 14850, USA

* Correspondence: ailong.ke@cornell.edu

Abstract: RNAs are prone to misfolding and are often more challenging to crystallize and phase than proteins. Here, we demonstrate that tRNA fusion can streamline the crystallization and structure determination of target RNA molecules. This strategy was applied to the T-box riboswitch system to capture a dynamic interaction between the tRNA 3'-UCCA tail and the T-box antiterminator, which senses aminoacylation. We fused the T-box antiterminator domain to the tRNA anticodon arm to capture the intended interaction through crystal packing. This approach drastically improved the probability of crystallization and successful phasing. Multiple structure snapshots captured the antiterminator loop in an open conformation with some resemblance to that observed in the recent co-crystal structures of the full-length T box riboswitch–tRNA complex, which contrasts the resting, closed conformation antiterminator observed in an earlier NMR study. The anticipated tRNA acceptor–antiterminator interaction was captured in a low-resolution crystal structure. These structures combined with our previous success using prohead RNA–tRNA fusions demonstrates tRNA fusion is a powerful method in RNA structure determination.

Keywords: RNA; riboswitch; structure; X-ray crystallography; crystal packing; RNA binding; base pair



Citation: Grigg, J.C.; Price, I.R.; Ke, A. tRNA Fusion to Streamline RNA Structure Determination: Case Studies in Probing Aminoacyl-tRNA Sensing Mechanisms by the T-Box Riboswitch. *Crystals* **2022**, *12*, 694. <https://doi.org/10.3390/cryst12050694>

Academic Editor: Blaine Mooers

Received: 5 April 2022

Accepted: 11 May 2022

Published: 13 May 2022

Publisher's Note: MDPI stays neutral with regard to jurisdictional claims in published maps and institutional affiliations.



Copyright: © 2022 by the authors. Licensee MDPI, Basel, Switzerland. This article is an open access article distributed under the terms and conditions of the Creative Commons Attribution (CC BY) license (<https://creativecommons.org/licenses/by/4.0/>).

1. Introduction

Besides serving as a central link to pass genetic information from DNA to protein, RNA is capable of adopting stable ternary structures to catalyze biochemical reactions, regulate gene expression in *cis*, and serve as structural scaffolds. Riboswitches manifested this theme excellently. Riboswitches regulate the expression level of the bacterial mRNA in *cis* in response to a specific cellular metabolite (for an excellent recent review on riboswitch function and diversity, see [1]). Regulation generally occurs at the level of premature transcription termination or translation initiation, involving ligand-dependent conformational changes; other mechanisms exist, such as regulating mRNA stability [2].

Considerable effort has been devoted to characterizing the structure–function relationship in riboswitches in order to understand their ligand recognition and the conformational switching mechanisms. The most productive method to provide such high-resolution structural information has been X-ray crystallography. Like many challenges encountered in early protein crystallography, obtaining diffraction-quality crystals remains quite challenging for RNA due to its irregular shape and higher conformational flexibility in RNA [3–5]. To overcome these challenges, RNA engineering is a crucial part of most RNA structure determination efforts, and several proven strategies now exist [5–7]. Often, targets are chosen from more stable RNA structures from thermophilic organisms, construct length

is minimized, distal helices and loops not directly involved in function are shortened, simplified, or replaced with known stable motifs that serve as crystallization contacts (i.e., the GAAA tetraloop), and stabilizing mutations are made. Another strategy is to bind stabilizing elements to the target RNA as a crystallization chaperone. U1A-binding motifs and K-turns have been introduced into nonessential regions of RNAs and the resulting fusion RNA displayed improved crystallization and X-ray diffraction properties when in complex with U1A- or K-turn-binding protein, respectively [6,8–12]. A similar approach is to raise Fab antibody fragments to stabilize structures and thanks to modern panning methods, this technique is becoming more feasible [13–18]. Post-crystallization approaches including cation replacement and dehydration have also shown considerable success for improving diffraction quality [19,20].

The use of crystallization chaperones is also instrumental in protein crystallography; however, many chaperone proteins are covalently fused with the target protein, either at termini or internal loops, to prevent chaperone dissociation during crystallization [3,21–24]. Analogously, we show that tRNA can be a useful crystallization chaperone when covalently fused to the target RNA molecule. The ability of tRNAs to form higher-ordered scaffolds is demonstrated by their behavior in crystals. The first RNA structure determined using X-ray crystallography was that of yeast tRNA_{Phe} in 1973 [25] and many additional tRNA structures have since been determined. The crystal packing interactions formed by tRNAs have been well characterized. Our choice to use tRNA as a crystallization chaperone is based on prior knowledge that tRNA folds robustly strong evolutionary pressure to conserve its structure; the inspection of other tRNA crystal structures revealed strong and predictable crystal contacts and engineered tRNA fusions have shown drastically improved folding and stability when expressed in vivo [26–29]. We have previously employed tRNA fusions to determine the structure prohead RNA (pRNA) domain II structure [30,31]. We hypothesized that we could use an engineered tRNA scaffold to assist the crystallization of the usually dynamic T-box antiterminator and to potentially select tRNA acceptor–antiterminator interactions in crystals. Here, we present our engineering workflow and the three resulting structures of tRNA–antiterminator fusions that provide insight into the conformational flexibility in the antiterminator and potential mechanisms for tRNA acceptor recognition. We have now successfully applied this strategy to multiple systems in our laboratory and believe the tRNA module offers more opportunities to form stable crystal contacts capable of trapping dynamic target RNAs in one or more conformations suited for crystal growth and high-resolution X-ray diffraction analysis.

2. Materials and Methods

Construct design, RNA transcription, purification, and refolding—The scaffold for tRNA fusions was the core of the *G. kaustophilus* tRNA_{Gly} that we previously published [32]. Constructs were designed using a rational approach for modelling with folding predictions performed using the Mfold webserver, such that intended secondary structures were predicted to be maintained [33]. tRNA sequences were PCR amplified by nested PCR and cloned into a modified pUC vector to include the T7 promoter and a 3′ HDV ribozyme [4]. For crystallization, each modified tRNA fusion was PCR amplified from the pUC vector using a generic 5′ (AAAAGAATTCTAATACGACTCACTATAGCGGAAGTAGTTCAGTG-GTAGAACAC) and 3′ primer (either T [2′ O-methyl-G] GAGCGGAAGACGGGACTC for a UCCA tail or T [2′ O-methyl-G] CCGCGGAAGACGGGACTC) for a UCGG tail. The amplified PCR products were used directly as a template for T7 RNA polymerase run-off transcription, with the 2′ O-methyl modification incorporated to reduce 3′ end variability [34]. Transcription was performed as previously described [4]. RNAs were separated by urea denaturing gel electrophoresis, excised from the gel by eluting into ddH₂O. Eluted RNAs were then buffer exchanged to removed contaminating gel materials and exchanged into a minimal 10 mM HEPES buffer (pH 7.0) with 50 mM NaCl. tRNA fusions were refolded by heating to 92 °C for 2 min, cooled to 65 °C before adding 10 mM MgCl₂, and rapidly cooled on ice. The folding protocol was monitored using native polyacrylamide gel

electrophoresis. tRNA fusions were concentrated using Millipore centrifugation columns and either used directly in crystallization plates or flash frozen in liquid nitrogen.

Crystallization and data collection—Crystallization conditions were screened using 96-well sitting drop plates with a 1:1 RNA solution to reservoir solution ratio using the Natrix HT and Nucleic Acid Mini-screens (Hampton Research, Aliso Viejo, CA, USA). Data sets were collected from four different tRNA–antiterminator fusions. Construct #4 crystals were optimized in 50 mM sodium cacodylate pH 6.0, 80 mM KCl, 12 mM spermine, 20 mM BaCl₂, 15% 2-methyl-2,4-pentanediol and cryoprotected by supplementation with 10% ethylene glycol. Construct #5 crystals were optimized in 10 mM MgCl₂, 50 mM Tris-HCl pH 7.5, 1.6 M Ammonium sulfate and cryoprotected by supplementation with 20% ethylene glycol. Construct #19 crystals were optimized in 10% 2-methyl-2,4-pentanediol, 40 mM sodium cacodylate pH 7, 12 mM spermine hydrochloride, 40 mM lithium chloride, 80 mM strontium chloride, 20 mM magnesium chloride and cryoprotected by supplementation of the well solution with 15% ethylene glycol. Data were collected at the Advanced Photon Source on the NE-CAT beamlines 24-ID-E.

Data processing and structure solution—Data were processed using XDS [35], Pointless, and Scala [36] in the RAPD pipeline developed at the NE-CAT facility at the Advanced Photon Source. Data processing details are shown in Table 1. The relatively conservative resolution cut-offs were determined by evaluating CC1/2 and $I/\sigma I$ values. The resolution cut-offs for both high-resolution structures were chosen just below the point that CC1/2 values rapidly declined while $I/\sigma I$ was greater than 1.5. Data were phased using Phaser-MR [37] from the Phenix program suite [38] with our previously determined *G. kaustophilus* tRNA_{Gly} structure (PDB ID: 4MGM) as a search model [32]. All manual structure building was performed using Coot [39] and the RCrane extension [40]. Refinements were performed using PHENIX.Refine [41] or Refmac [41] and Rosetta ERRASER [42] was used to improve model building, giving the limited resolution of the data. Structure figures were generated in PyMol (The PyMOL Molecular Graphics System, Version 2.0 Schrödinger, LLC, New York, NY, USA).

Table 1. X-ray data collection and processing statistics.

/	Anti-tRNA Construct 4 UCCA -2bp	Anti-tRNA Construct 19 Flip UCCA	Anti-tRNA Construct 5 MOD FL
Data collection ^a	/	/	/
Beamline	APS 24ID-E	APS 24ID-E	APS 24ID-E
Wavelength (Å)	0.979	0.979	0.978
Resolution range (Å)	32–2.95 (3.11–2.95)	33.6–3.03 (3.14–3.03)	45.8–6.1 (6.45–6.12)
Space group	C222 ₁	C222 ₁	P6 ₁ 22
Unit cell dimensions (Å)	<i>a</i> = 88.6, <i>b</i> = 165.2, <i>c</i> = 57.1	<i>a</i> = 46.2, <i>b</i> = 56.7, <i>c</i> = 268.9	<i>a</i> = 168.5, <i>b</i> = 168.5, <i>c</i> = 136.3
Unique reflections	9103 (1263)	7208 (688)	2948
Completeness (%)	99.5 (97.5)	99.2 (98.6)	99.3 (99.7)
Multiplicity	6.2 (4.9)	7.1 (7.3)	9.8 (10.1)
Average $I/\sigma I$	18.9 (3.2)	12.9 (1.6)	13.6 (1.3)
R_{merge}	0.115 (0.552)	0.131 (1.135)	0.136 (1.991)
$R_{\text{p.i.m.}}$	0.055 (0.277)	0.053 (0.446)	0.047 (0.673)
CC1/2	0.942 (0.808)	0.997 (0.991)	0.998 (0.351)
Refinement	/	/	/
R_{work} (R_{free})	24.7 (26.5)	24.6 (27.6)	/
<i>B</i> -factors (Å ²)	/	/	/
All atoms	63.3	100.7	/
RNA	63.0	100.3	/
Ions	100.2	144.57	/
r.m.s.d. bond length (Å)	0.002	0.005	/
r.m.s.d. bond angle (°)	0.536	0.95	/
PDB Accession Codes	7UQ6	7UZ0	/

^a Data in parentheses represent the highest-resolution shell.

3. Results

3.1. Challenges in Crystallizing the tRNA/T-Box Antiterminator Complex Inspired the Design of tRNA–Antiterminator Fusions

The T-box family of riboswitches are quite unique because they bind tRNA and sense its aminoacylation status to regulate downstream genes, typically amino acid synthetases and importers (Figure 1A) [43,44]. Despite being studied for more than 30 years, the high-resolution T-box riboswitch–tRNA complex structure has only recently been determined [45–47]. T-box riboswitches can be grouped into two related structural motifs, depending on whether they regulate at the level of transcription or translation. For an excellent recent review of the structure and function of the structural elements from these two classes, see Zhang 2020 [48]. In brief, Stem I decodes the tRNA, forming the codon–anticodon interaction and other docking interactions with tRNA [12,32,49–51]. Stem 1 is followed by a variable region that can include two additional stems, though in the well-characterized tRNA_{Gly} sensing switches that have been the focus of most structural studies, these stems are absent or minimal [52,53]. The variable regions are important for stabilizing and orienting other important structural elements of the T-box riboswitch and also form important interactions with tRNA directly [45–47]. The final stem, together with Stem III form the antiterminator or discriminator that transitions between either a terminator/antiterminator or a sequesteror/antisequesteror and senses the aminoacylation status of the bound tRNA [43,54].

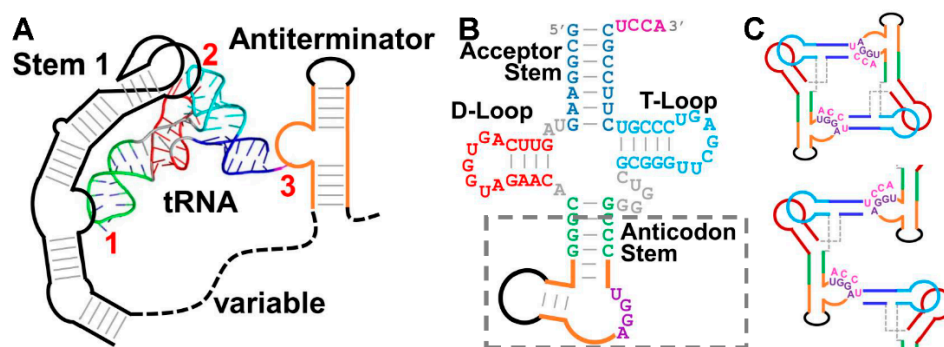


Figure 1. Engineering tRNA fusions. (A) Schematic of the T-box riboswitch–tRNA complex with the three previously demonstrated intermolecular contacts highlighted by red numbers. The conserved T-box structure is shown schematically with stems indicated by grey base pairs and loops and bulges shown unpaired. The antiterminator portion of the T-box RNA that is the focus of this work is highlighted in orange. The more variable region of the T-box structure is indicated by a dashed line. tRNA is shown as a cartoon with the acceptor stem in blue, the D-loop in red, the anticodon stem loop in green, the T-loop in cyan and the 3' acceptor extension in magenta. (B) Secondary structure model of the *G. kaustophilus* tRNA_{Gly} scaffold used in this work, colored as in Panel A, with antiterminator stem-loop insertions (highlighted by a dashed grey box) in the anticodon stem represented by orange lines. The UGGA motif (purple) in the antiterminator single-stranded bulge is the tRNA acceptor (UCCA) binding site from the T-box riboswitch antiterminator. (C) Potential intermolecular complexes hypothesized, either dimeric (top) or bridging (bottom) during engineering of the tRNA–antiterminator fusion. tRNA molecules are shown schematically and colored as in Panel B.

A structure of a minimal antiterminator stem was determined by NMR, revealing important structural features for display of the tRNA acceptor recognition sequences [55] and more recently, structures of the full-length T-box riboswitches, a tRNA–discriminator complex and several biophysical approaches revealed key details regarding the interaction of the tRNA acceptor and the discriminator [45–47,56–58]. Together, these data support a model for tRNA sensing, where tRNA first rapidly binds to the Stem 1 structure through a sequence-specific codon–anticodon interaction and is stabilized against the stem by structurally specific docking between the distal Stem 1 loops and the tRNA D- and T-

loops [5,59,60]. With tRNA anchored to the mRNA leader, an antiterminator is stabilized by base pairing between the uncharged tRNA UCCA 3' tail and a UGGA sequence in the antiterminator bulge and co-helical stacking between the acceptor helix and the antiterminator helix (Figure 1A) [45–47,61–65]. Aminoacylated tRNA binds Stem 1 but is unable to stabilize the antiterminator, allowing a transcription terminator to form and favoring tRNA release.

Prior to the publication of high-resolution full-length T-box riboswitch–tRNA structures, our attempts to assemble a stable tRNA–antiterminator complex on its own were unsuccessful. Numerous constructs were examined, including simplified versions of the antiterminator stem with shortened, stabilized helices, exchanging the terminal loop for a GAAA tetraloop and simplified tRNAs, including constructs to mimic the acceptor stem alone, capped with a GAAA tetraloop. Ultimately, these crystallization efforts were not successful, likely hampered by the dynamic nature of this interaction. We hypothesized that if we created an artificial fusion between tRNA and the T-box antiterminator, there is a possibility that the intended 1:1 tRNA–antiterminator complex may be captured in crystal contacts, where the tRNA acceptor from one fusion molecule contacts a crystallographically related antiterminator domain. This idea was inspired by the existing literature showing that tRNA is a robust, widespread RNA fold [66–68]. The general tRNA fold is conserved throughout all domains of life and remnants of the fold exist in other structured RNAs, including tmRNA [69], the tRNA-like structure (TLS) found at the 3' end of the Turnip Yellow Mosaic Virus (TYMV) [70], and Y RNA [71]. tRNA is composed of the acceptor stem (with a UCCA 3' tail that becomes aminoacylated), the D-loop, the anticodon stem-loop, and the T-loop (Figure 1B). This “cloverleaf” secondary structure folds into an L-shaped three-dimensional structure with the D- and T-loops interacting at the elbow and the acceptor and anticodon stems protruding from either arm of the “L” (Figure 1A). This stable fold is also ideally suited, due to its biological roles, to form RNA–RNA complexes through specific base pairing to the anticodon and through base stacking against the D- and T-loop platforms and the terminus of the acceptor helix. Additionally, circularly permuted tRNAs and anticodon and acceptor arm mimics have been used to study translation mechanisms and in several RNA structure–function studies [12,72–76]. Fusing an RNA of interest to tRNA via its anticodon stem has been shown to consistently improve its in vivo folding and stability [28]. We initially designed fusion constructs based on in silico modeling using known tRNA structures and the antiterminator NMR structure [55], but ultimately screened numerous constructs, summarized in Figure 2. We hypothesized that we could either develop a construct that formed closed dimers across complementary acceptor stems and antiterminators, or that the acceptor–antiterminator interaction would stabilize higher-ordered interactions observed through crystal packing. We solved three different tRNA–antiterminator fusion structures and in all cases, the core tRNA structure closely resembles the published *G. kaustophilus* tRNA_{Gly} structure with only minor differences [32]. Here, we will begin by discussing our iterative engineering approach to optimizing constructs and attaining diffraction-quality crystals before providing a more in-depth analysis of the structures themselves.

To begin to design tRNA–antiterminator fusion for crystallization, we first sought to minimize the structure. Our starting point was the full-length antiterminator from the *G. kaustophilus* tRNA_{Gly} T-box riboswitch that has been the model for most of our previous work [5,30–32,49,59]. The *G. kaustophilus* antiterminator resembles canonical antiterminators with a proximal helix, broken by a single-stranded bulge that contains the tRNA UCCA tail recognition sequence, UGGA and a distal helix capped by a loop. To simplify the structure, both helices were shortened, and G–C base pairs were incorporated to stabilize the shortened helices. The broadly utilized GAAA tetraloop was also incorporated into the distal helix to provide a stable turn with a known propensity to form crystal contacts. This led us to Constructs #1–4, where the only variable was the length of the anticodon helix linking the tRNA scaffold to the antiterminator (Figure 2). This was varied to alter the direction and distance of the antiterminator bulge relative to the tRNA. From this initial set of

constructs, our first well-diffracting crystals were obtained from Construct #4. The structure was easily solved using molecular replacement with analogous fragments from our previous *G. kaustophilus* tRNA_{Gly} crystal structure (PDB ID: 4MGM) as the search model [32]. After phasing, a clear density for the engineered antiterminator inserts were observed in all data sets. To our disappointment, the targeted tRNA acceptor arm/antiterminator bulge interaction was not observed, so we altered our starting model to favor the interaction (see information below and Figure 3). Interestingly, the resulting antiterminator domain, and those from later tRNA fusion structures, adopted an unexpected conformation distinct from the previously determined antiterminator NMR structure [55]. This is analyzed in detail later.

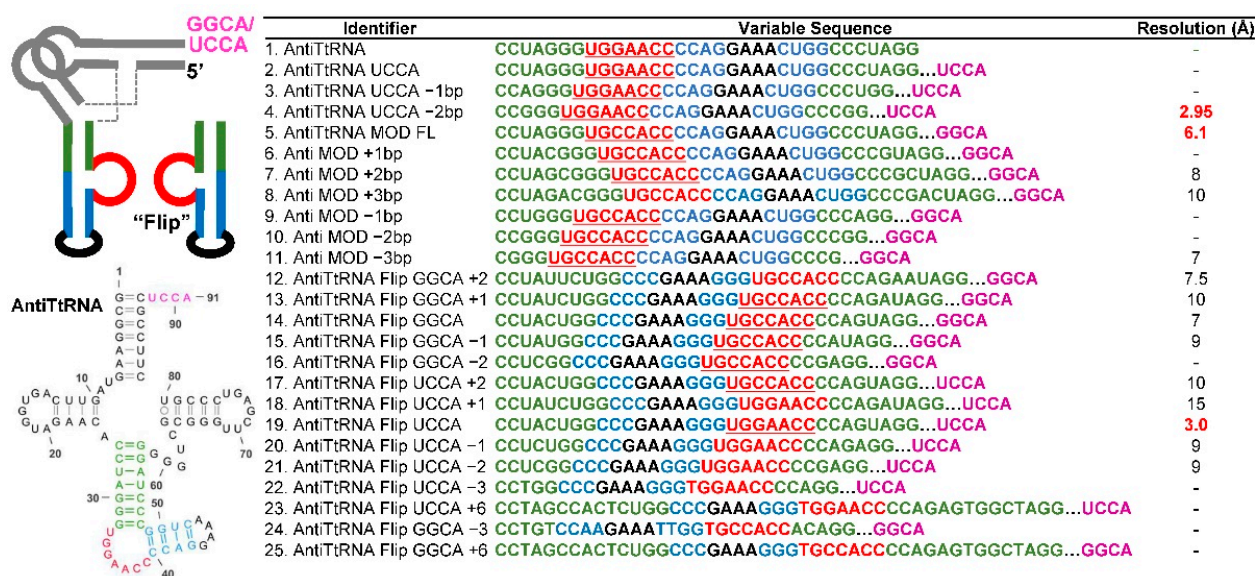


Figure 2. tRNA-antiterminator fusion designs. The core *G. kaustophilus* tRNA_{Gly} structure remained consistent across designs with insertions restricted to the anticodon stem (green), colored as in the structural schematic (top) and secondary structure model (bottom, Construct #1, AntiTtRNA shown) on the left panel with the single-stranded bulge (red) either on the 5' side or 3' side of the inserted stem loop, capped by a GAAA tetraloop (black). The 3' end of the tRNA also includes either a typical UCCA tail or an engineered GGCA tail (magenta). Resolution listed on the right column represents predicted diffraction limits from two orthogonal diffraction images from crystals pulled directly from sparse matrix crystal screens (black font). Red font indicates crystal constructs for which full data sets were collected. A dashed line indicates constructs that either did not crystallize or did not yield crystals of sufficient quality for looping and testing.

We took two separate approaches to promote the targeted complex formation. The first approach was to strengthen the potential base pairing between the tRNA acceptor and the antiterminator by replacing the UCCA tRNA acceptor tail with GGCA and making the complementary UGGA to UGCC substitution in the antiterminator. These complementary modifications maintain the length of the Watson–Crick base paired interaction, but an A–U base pair was replaced with a G–C pair to increase stability. This group of modifications led to a low-resolution structure (Figure 2, Construct #5) that was solved by molecular replacement and the crystal packing is such that the targeted interaction could form. However, despite significant effort, diffraction could not be improved to a suitable resolution to definitively model the tRNA acceptor–antiterminator interaction.

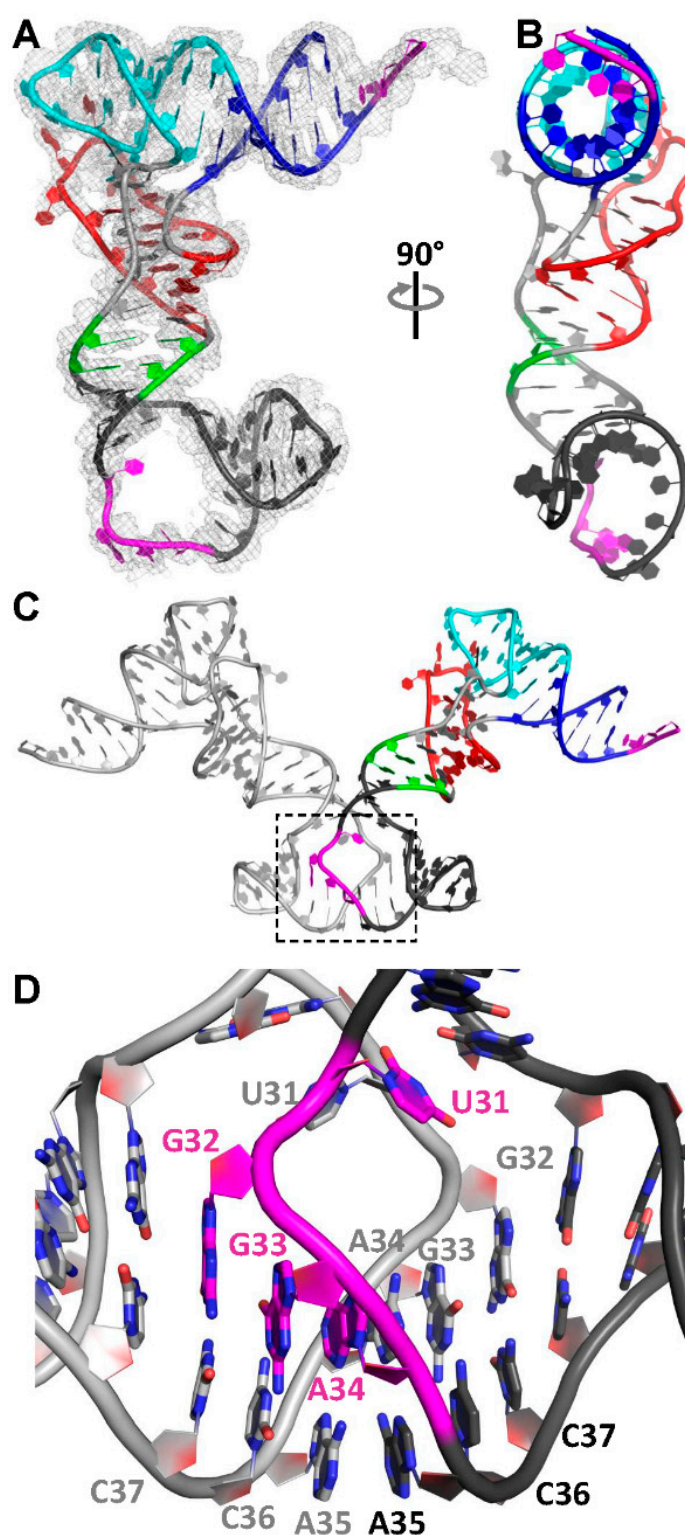


Figure 3. The 2.95 Å resolution crystal structures of tRNA-antiterminator fusion Construct #4 in space group C222₁. (A) Cartoon representation with 2F_o-F_c electron density contoured at 1.0 σ, shown as a mesh. (B) Part A rotated 90° and shown without electron density. (C) Overall structure crystal packing across the antiterminator bulge and (D) close-up of the antiterminator bulge interactions highlighted by the dashed box in Panel C. Nucleotide numbering corresponds to numbering in the full-length construct. Coloring as in Figure 1 schematic, with the acceptor stem (blue), D-loop (red), T-loop (cyan), anticodon stem (green), antiterminator insertion (black), and the T-box sequence and tRNA UCCA tail (magenta).

The second approach we used to favor the targeted complex was to fuse the antiterminator domain to tRNA in a circularly permuted fashion, with the tRNA attached to the loop end of the antiterminator, rather than to the stem base. The reason for this counterintuitive fusion design was to orient the antiterminator bulge in an orientation that might favor the formation of a head-to-tail tRNA–antiterminator dimer. To direct the bulge in the same direction as the tRNA acceptor arm, an obvious approach would be to lengthen or shorten the anticodon stem to rotate the bulge around the RNA helix, but to avoid adding unnecessary length to extend the helix to rotate another 90–180°, we designed a “flipped” antiterminator in which the bulge was located on the 3′ end of the distal helix rather than the 5′ end (Figure 2, Constructs #12–21). Moving the bulge also required the circular permutation of the T-box interaction motif to restore antiparallel base pairing between the UCCA/UGGC tail. This design should place the bulge on the same face of the helix as the acceptor stem, which was indeed observed in the 3.0 Å resolution structure determined using Construct #19 (see description below). However, again the targeted interaction was not observed. This level of iterative engineering is common during any typical RNA structure determination effort. The fact that we obtained two different, well-diffracting crystal forms for a challenging target with little condition optimization or post-crystallization manipulation was encouraging. Upon recognizing how powerful this fusion approach was to structure determination in general, we abandoned further engineering to select for our desired complex and instead focused on analyzing the insight we could glean from our two high-resolution structures and to focus on applying the tRNA fusion method to other structured RNAs of interest.

3.2. The Structure of a Minimal tRNA–Antiterminator Fusion (Construct #4)

Because crystal lattice interactions are difficult to predict, we used an iterative approach to design, produce and optimize the crystallization constructs. The initial designs (constructs #1–4) used the native tRNA UCCA 3′ tail and the anticodon stem lengths were varied. Well-diffracting crystals were obtained from Construct #4 and the structure was determined to 2.95 Å resolution (Figure 3A,B and Supplementary Materials Figure S1). The data quality was good, the structure was easily phased using molecular replacement with the previously determined *G. kaustophilus* tRNA_{Gly} structure (PDB ID: 4MGM) with its anticodon loop removed. Continuous electron density for all nucleotides, including the entire antiterminator that was absent from the search model, was observed, excluding the last A87 from the UCCA tail (see Supplementary Materials Figure S2).

This construct crystallized in the space group C222₁ with one molecule in the asymmetric unit. Symmetry-related molecules formed crystal contacts by stacking neighboring D-T-Loops against one another and through mutual interactions from the antiterminator loop to the same antiterminator loop of a symmetry-related molecule, in a kissing–bulge interaction (see Supplementary Materials Figure S3). Notably, the propensity for antiterminators to form kissing bulges in solution was previously observed and the NMR structure carries a single point mutation in the bulge to inhibit dimer formation [55,63]. The antiterminator fusion is oriented such that the antiterminator bulge is directed out the opposite face of the tRNA to the acceptor stem (Figure 3A,B). The bulge is in an extended conformation, creating an ~90° bend to extend the distal antiterminator stem and GAAA tetraloop in the same direction as the tRNA acceptor stem. The extended conformation of the bulge is stabilized by interaction with the bulge of its symmetry mate (Figure 3C,D). All bases in the bulge are exposed to intermolecular contacts in this conformation, and they form imperfectly paired Watson–Crick base pairs with the bulge residues in a crystal symmetry mate. The interacting RNAs run antiparallel to each other, as expected for the biological acceptor–antiterminator interaction, but U31 is directed away from the interaction into the open space of the bulge and potentially forms a stacking interaction with U31 from a symmetry-related molecule (Figure 3D). The remainder of the acceptor recognition motif, G32, G33 and A34, forms Watson–Crick pairs with the symmetry-related C37 and C36 and a sugar–Hoogsteen pair with A35, respectively. This interaction is extended across the

loop by symmetry where A35, C36 and C37 for the molecule in the asymmetric unit base pairs to the symmetry-related acceptor recognition motif, A34, G33 and G32, respectively. The result of this extensive base-pairing scheme is an extended co-helical stack from the GAAA tetraloop of one distal antiterminator stem-loop to the distal GAAA tetraloop of its symmetry mate with the extended helix formed through the interacting bulges (Figure 3D). Interestingly, the conformation of the antiterminator domain in this crystal form is consistent with that in our later crystal structure but differs significantly from that in the antiterminator NMR structure (see Supplementary Materials Figure S4) [55]. In both the NMR and our crystal structure, the 7 nt bulge imparts a similar $\sim 90^\circ$ kink between the proximal and distal helices; however, the bulge itself adopts an open conformation in the crystal structures to welcome base-pairing interactions, whereas the equivalent region in the NMR structure is in a partially occluded conformation. In the conformation of the NMR structure, tRNA binding to the antiterminator would require conformational rearrangement, as recognized by the authors [55]. While the NMR structure likely reveals the most stable resting structure of a monomeric antiterminator, our crystal structure is much closer to the conformation of the tRNA-bound form, with an open antiterminator bulge bound by an RNA duplex with at least a 4-nt 3'-overhang (Figure 4A). The observed interaction is stabilized by forming an extended helix with the distal antiterminator helix (Figure 3C). While the antiterminator bulge opens up similarly among the co-crystal structures and the engineered tRNA–antiterminator fusions, the bases rotate out to expose their Watson–Crick edges in opposite orientations. The final conformation of GGA is similar, though U turns inward, likely due to steric hinderance by the crystal symmetry interaction (Figure 4B). While this structure does not directly demonstrate the targeted acceptor–antiterminator interaction, the overall conformation of the antiterminator bulge and the similar co-axial stack with the antiterminator distal stem-loop while the UCCA tail interacts with the antiterminator UGGA resemble that of the high-resolution complexes. At this point, we chose to focus on engineering the structure to stabilize the target complex.

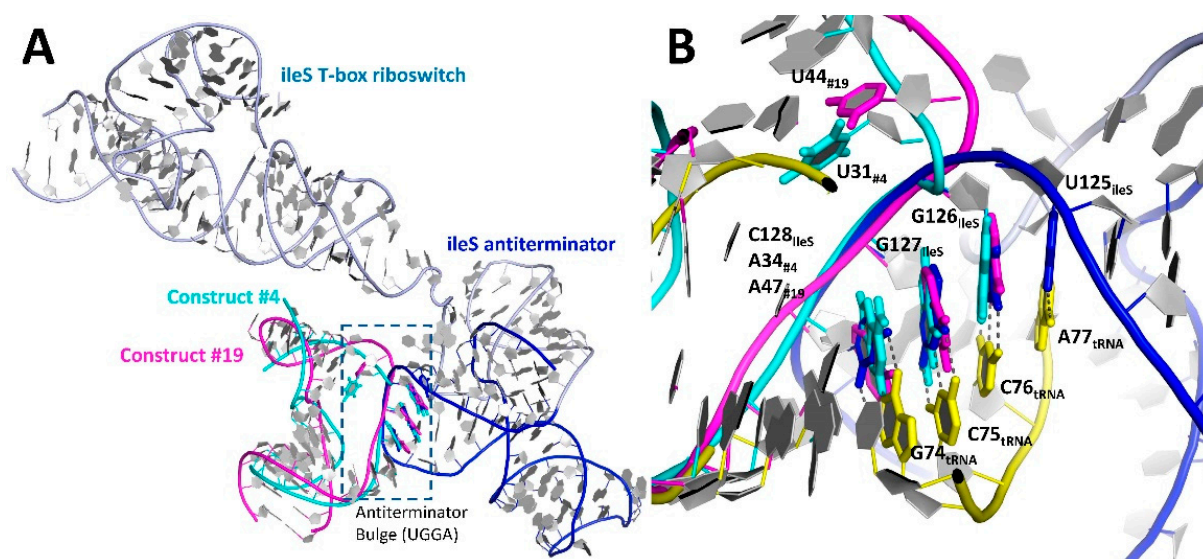


Figure 4. Comparison of the fusion antiterminator and ileS T-box riboswitch-tRNA co-crystal structures. (A) The tRNA acceptor stem-binding bases, UGGA, were superposed from the ileS T-box riboswitch structure (light blue, PDB ID: 6UFG), and the structures of Constructs #4 (cyan) and #19 (magenta). The antiterminator bulges are highlighted by a dashed box. (B) Close up of the UGGA motif from the antiterminator bulge and its interaction with tRNA (yellow) in the ileS T-box riboswitch structure. Nucleotides are numbered according to numbering in deposited coordinate files and are colored as in Panel A.

3.3. Relocation of the Antiterminator Bulge to the 3' Side of the Stem-Loop

To rotate the orientation of the antiterminator bulge to the other side of the RNA helix and favor a closed dimer, we engineered the bulge at the 3' side of the antiterminator stem (Figure 2, Constructs #12–21). Well-diffracting crystals were obtained for this “flipped” bulge design with a UCCA tail and a full-length anticodon stem (Construct #19, AntiTtRNA Flip UCCA). Data were processed to 3.0 Å resolution in space group C222₁ with different cell dimensions than the previous C222₁ structure. Like the previous solution, the data were readily solved by molecular replacement using the trimmed *G. kaustophilus* tRNA_{Gly} crystal structure (PDB ID: 4MGM) and nucleotides in the unmodeled regions were readily interpretable. Since the stem was 2 bp longer than Construct #4, the bulge extends approximately 90° from the direction of the tRNA acceptor arm (Figure 5). Like the first fusion structure, the bulge forms an extended interaction with the distal antiterminator helix, which is bent ~90° from the direction of the anticodon stem. Interestingly, like the 5' side bulge, the first base, U44 (equivalent to U31 in Construct #4) is directed inward toward the center of the bulge, to stack with A43 from an A-U Watson–Crick base pair at the base of the distal stem (Figure 5D). Most notably, the remaining bases in the antiterminator bulge (45–50) rotate completely out, forming continuous symmetric WC and non-WC base pairs with the equivalent region of a symmetry molecule (with C45-G50_{SYM1}, A46-U49_{SYM1}, A47 interacting with A48_{SYM1}, A48 with A47_{SYM1}, U49-A46_{SYM1}, and G50-C45_{SYM1}) (Figure 5D and Supplementary Materials Figure S5). The orientation of this loop away from the antiterminator, with WC edges solvent exposed, is a similar overall orientation to the previous structure (Construct #4). A third contact from the antiterminator distal GAAA tetraloop of another symmetry-related molecule interacts with the bulge, docking in the minor groove of the intermolecular helix at base pairs C45-G50_{SYM1} and A46-U49_{SYM1}, forming base triples or contacts with 2'-OH from the antiterminator bulge of symmetry mates. A40 of the symmetry tetraloop forms a sheared A-minor interaction with A46-U49_{SYM1}. The interesting crystal contacts forming with the rest of the molecule occur through the tRNA D- T-loops stacking against the first base pair in the tRNA acceptor stem G1-C87. While these high-resolution structures did not trap our targeted tRNA 3' tail–antiterminator complex, the conformations and base pairing from the antiterminator bulge reveal several characteristics about how the bulge interacts with target tRNA to sense aminoacylation.

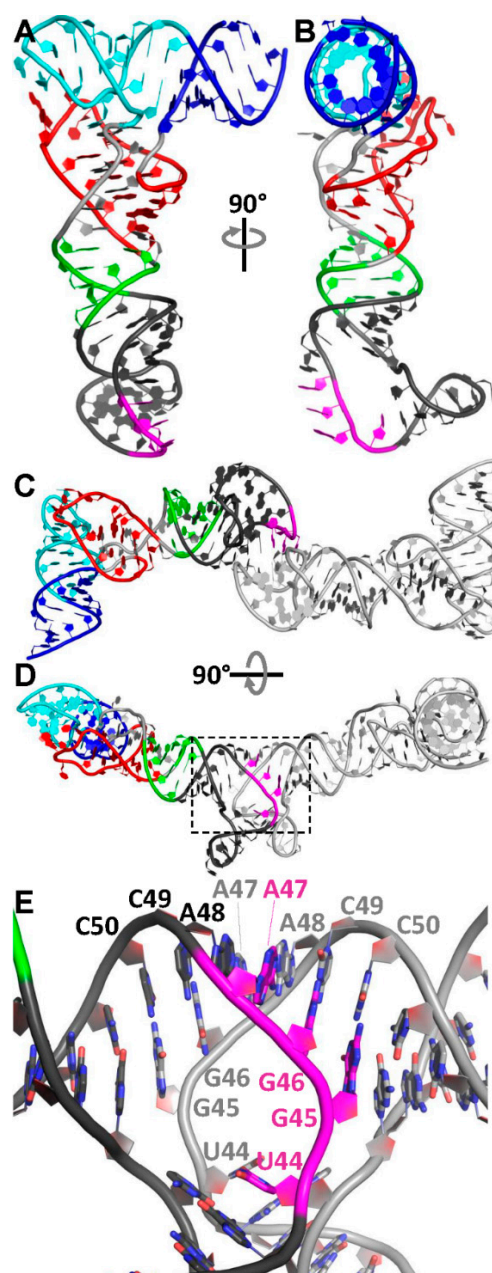


Figure 5. The 3.0 Å resolution crystal structures of tRNA-antiterminator Construct #19 in space group C222₁. (A) Cartoon representation of the overall structure. (B) Part A rotated 90°. (C) Overall structure of crystal packing at the antiterminator bulge. (D) Part C rotate 90°. (E) Close-up of the antiterminator bulge interactions highlighted by the dashed box in Panel D. Nucleotide numbering corresponds to numbering in the full-length construct. Coloring as in Figure 1 schematic.

3.4. Phasing of a Low-Resolution Interaction between the tRNA Acceptor and Antiterminator

Armed with two high-resolution tRNA-antiterminator fusion models, we were able to phase a low-resolution crystal form using molecular replacement that appears to possess the targeted interaction. Construct 5 possessed the modified tRNA 3' GGCA and its complementary antiterminator UGCC. Despite repeated attempts to improve X-ray diffraction, the best data set was processed to 6.1 Å resolution. Crystals formed in space group *P*6₁22 with one molecule in the asymmetric unit. A clear molecular replacement solution was obtained that reveals the targeted tRNA acceptor-antiterminator bulge interaction between symmetry-related molecules. The initial $2F_o - F_c$ and $F_o - F_c$ electron density following rounds of rigid-body refinement revealed continuous electron density and a large positive peak

protruding from the tRNA acceptor stem 3' end into the antiterminator bulge (Figure 6). A tightly constrained model was built using ideal geometry to gain insight into the complex. Unfortunately, due to the limited resolution, the interactions between the antiterminator and CCA tail could not be definitively modelled. Further efforts to improve the resolution of this crystal form have so far been unsuccessful, but these results are promising and indicate that our rational design approach could lead to the capturing of the intended interaction.

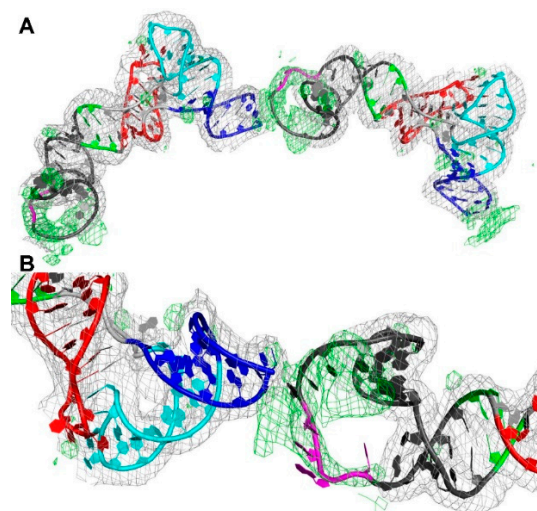


Figure 6. The 6.1 Å resolution maps and preliminary model for the tRNA acceptor–T-box antiterminator interaction in space group $P6_122$. (A) Overall structure of the complex formed through crystal symmetry and (B) close-up of the trapped tRNA UCCA–antiterminator interaction. The structure was solved by molecular replacement with core tRNA scaffold and the terminal GAAA-tetraloop. After a round of rigid body refinement, omit $2F_o-F_c$ (grey, contoured at 1.0 σ) and F_o-F_c (green, contoured at 2.5 σ) maps are shown as mesh. The complete model was placed in the density by fusing the 2.95 Å resolution Construct #4 structure antiterminator in the molecular replacement model. The unmodelled region is drawn with bases removed in part A.

3.5. The tRNA Scaffold Is a Powerful Tool for RNA Structure Determination

Several observations during tRNA–antiterminator fusion work led us to conclude that the tRNA scaffold could serve as a powerful tool for RNA structure determination: (A) We had previously been unsuccessful at crystallizing the antiterminator but fusing it to tRNA dramatically improved the chance of crystallization. (B) Because tRNA folding is very robust, it may prevent target RNA misfolding by restricting alternative folding pathways. (C) Phasing RNA structures can be challenging but the stably folded tRNA scaffold makes phasing by molecular replacement straight forward. (D) The combination of the above factors led to very efficient RNA structure determination pipeline, drastically reducing the effort of solving an RNA structure. Clearly, the tRNA scaffolding approach is a powerful tool for RNA structure determination. We also used a simplified tRNA scaffolding approach for other RNA structural targets that have resisted other crystallization efforts in the lab, including the previously discussed phi-29 DNA packaging motor [30,77,78]. This technique has become a key method in our lab when characterizing RNAs that prove difficult to crystallize.

4. Discussion

RNA structure determination remains challenging. Here, we demonstrate the utility of using tRNA fusions to stabilize dynamic RNAs, provide crystal packing interfaces and to easily phase new structures using molecular replacement. The tRNA fusion strategy can be an extremely powerful addition to the RNA structure determination toolkit, particularly for RNAs that form small hairpins, are generally dynamic or poorly folded, or for studying

small changes to a given RNA molecule, such as the consequence of nucleotide substitution or chemical modification.

The biological roles of tRNA and its functional interfaces make it well suited to form intermolecular interactions for RNA crystal growth. One of the notable features of tRNA crystals is the observation of only a few different molecular packing interactions. These interactions typically involve the regions of the molecule that have biological functions in RNA recognition: the acceptor stem, the anticodon loop, and the stacking surface at the D- and T-loops. Generally observed crystal contacts are kissing-loop interactions through anticodon loops, the formation of an extended stacked helix by extension along the acceptor arm/T-loop direction by base stacking at either end of the acceptor stem or D- T-loops, or by interactions along parallel helices from the acceptor stem [6,79,80]. We observed several of these previously identified tRNA crystal packing interactions within our engineered construct crystals. This predictability in tRNA packing will also aid in rational construct design as potential packing interactions and stem orientations can be readily modelled and used to guide the fusion strategy.

The high-resolution structures determined all had symmetry-related contacts across their antiterminator bulges. This is not too surprising since the region, by natural selection, is optimized for interaction with a four-nucleotide linear RNA. Notably, homodimer formation across palindromic antiterminator bulges was previously observed for the *B. subtilis* *tyrS* antiterminator and a single-point mutation was ultimately introduced into the bulge to stabilize a monomeric form and determine NMR structure [55,63]. Though we did not capture the tRNA acceptor–antiterminator bulge interactions in high resolution, we did see examples of mimics in our structures with a single-stranded antiparallel RNA binding across the bulge. Using calorimetry and fluorescence lifetime measurements, Zhang and Ferré-D'Amaré previously demonstrated that the tRNA acceptor end coaxially stacks on the T-box antiterminator helix to provide additional stability to the complex in addition to the base pairing [61]. Our crystal structures display coaxial stacking of the acceptor stem-mimic with the distal helix of the antiterminator, stabilizing the bend between the proximal and distal antiterminator helices at $\sim 90^\circ$ angle. This is consistent with the full-length structures of the T-box riboswitch tRNA structure both in crystal structures and in solution, as observed by small-angle X-ray scattering and cryo-EM [46,47,57,58]. Our low-resolution Construct 5 map and model demonstrates some success in the initial goal to trap the tRNA acceptor tail bound to the antiterminator. Unfortunately, the limited resolution restricts the level of detail gleaned from the structure and further optimization of this crystal form and guided engineering of the constructs is the focus of future work.

5. Conclusions

One of the most important facets of this work is the demonstration of the power of the tRNA-fusion approach in RNA structure determination. We have now successfully applied this approach to studying the T box antiterminator (this work) and the phi-29 packaging motor [30]. Engineered tRNA fusions can accommodate a wide range of insertions in their anticodon stem from minimal, to very complex structures, such as the 218-nucleotide IRES domain III, the 184-nucleotide full-length pRNA and even a 376-nucleotide construct from 23S RNA [28]. The flexibility to accommodate a wide range of insertions suggests this tRNA fusion approach could be applied to many diverse RNAs in structure determination.

Supplementary Materials: The following are available online at <https://www.mdpi.com/article/10.3390/cryst12050694/s1>. Figure S1: Secondary structure models for the starting AntiTtRNA construct and the three crystallized constructs with structures reported in the text. Figure S2: Electron density for tRNA–antiterminator Construct #4 structure. Figure S3: Comparison of antiterminator bulge conformations for the previously determined NMR structure (PDB ID:1N53) and Constructs #4 and #19. Figure S4: Crystal packing interactions observed for the structure of Construct #4. Figure S5: Crystal packing interactions observed for the structure of Construct #19.

Author Contributions: Conceptualization, J.C.G., I.R.P. and A.K.; methodology, J.C.G. and I.R.P.; formal analysis, J.C.G., I.R.P. and A.K.; writing—original draft preparation, J.C.G., I.R.P. and A.K.; writing—review and editing, J.C.G., I.R.P. and A.K.; funding acquisition, A.K. All authors have read and agreed to the published version of the manuscript.

Funding: This research was funded by National Institutes of Health, grant number GM118174 and GM116632. This work is based upon research conducted at the Northeastern Collaborative Access Team beamlines, which are funded by the National Institute of General Medical Sciences from the National Institutes of Health (P41 GM103403). The Eiger 16M detector on 24-ID-E beam line is funded by a NIH-ORIP HEI grant (S10OD021527). This research used resources of the Advanced Photon Source, a U.S. Department of Energy (DOE) Office of Science User Facility operated for the DOE Office of Science by Argonne National Laboratory under Contract No. DE-AC02-06CH11357.

Institutional Review Board Statement: Not applicable.

Informed Consent Statement: Not applicable.

Data Availability Statement: Structural data were deposited in the RCSB Protein Databank with accession codes 7UQ6 and 7UZ0.

Acknowledgments: We would like to thank Fran Ding and other members of the Ke lab for their support.

Conflicts of Interest: The authors declare no conflict of interest.

References

- McCown, P.J.; Corbino, K.A.; Stav, S.; Sherlock, M.E.; Breaker, R.R. Riboswitch diversity and distribution. *RNA* **2017**, *23*, 995–1011. [[CrossRef](#)] [[PubMed](#)]
- Garst, A.D.; Edwards, A.L.; Batey, R.T. Riboswitches: Structures and Mechanisms. *Cold Spring Harb. Perspect. Biol.* **2011**, *3*, a003533. [[CrossRef](#)] [[PubMed](#)]
- Holcomb, J.; Spellmon, N.; Zhang, Y.; Doughan, M.; Li, C.; Yang, Z. Protein crystallization: Eluding the bottleneck of X-ray crystallography. *AIMS Biophys.* **2017**, *4*, 557–575. [[CrossRef](#)] [[PubMed](#)]
- Ke, A.; Doudna, J.A. Crystallization of RNA and RNA-protein complexes. *Methods* **2004**, *34*, 408–414. [[CrossRef](#)]
- Grigg, J.C.; Ke, A. Structures of Large RNAs and RNA-Protein Complexes: Toward Structure Determination of Riboswitches. *Methods Enzymol.* **2015**, *558*, 213–232. [[CrossRef](#)]
- Zhang, J.; Ferré-D'Amaré, A.R. New molecular engineering approaches for crystallographic studies of large RNAs. *Curr. Opin. Struct. Biol.* **2014**, *26*, 9–15. [[CrossRef](#)]
- Peselis, A.; Serganov, A. ykkC riboswitches employ an add-on helix to adjust specificity for polyanionic ligands. *Nat. Chem. Biol.* **2018**, *14*, 887–894. [[CrossRef](#)]
- Ferré-D'Amaré, A.R. Use of the U1A protein to facilitate crystallization and structure determination of large RNAs. *Methods Mol. Biol.* **2016**, *1320*, 67–76. [[CrossRef](#)]
- Ferré-D'Amaré, A.R.; Zhou, K.; Doudna, J.A. Crystal structure of a hepatitis delta virus ribozyme. *Nature* **1998**, *395*, 567. [[CrossRef](#)]
- Baird, N.J.; Zhang, J.; Hamma, T.; Ferré-D'Amaré, A.R. YbxF and YlxQ are bacterial homologs of L7Ae and bind K-turns but not K-loops. *RNA* **2012**, *18*, 759–770. [[CrossRef](#)]
- Huang, L.; Lilley, D.M.J. The molecular recognition of kink-turn structure by the L7Ae class of proteins. *RNA* **2013**, *19*, 1703–1710. [[CrossRef](#)] [[PubMed](#)]
- Zhang, J.; Ferré-D'Amaré, A.R. Co-crystal structure of a T-box riboswitch stem I domain in complex with its cognate tRNA. *Nature* **2013**, *500*, 363–366. [[CrossRef](#)] [[PubMed](#)]
- Ravindran, P.P.; Heroux, A.; Ye, J.D. Improvement of the crystallizability and expression of an RNA crystallization chaperone. *J. Biochem.* **2011**, *150*, 535–543. [[CrossRef](#)] [[PubMed](#)]
- Bailey, L.J.; Sheehy, K.M.; Dominik, P.K.; Liang, W.G.; Rui, H.; Clark, M.; Jaskolowski, M.; Kim, Y.; Deneka, D.; Tang, W.J.; et al. Locking the Elbow: Improved Antibody Fab Fragments as Chaperones for Structure Determination. *J. Mol. Biol.* **2018**, *430*, 337–347. [[CrossRef](#)]
- Koirala, D.; Shelke, S.A.; Dupont, M.; Ruiz, S.; DasGupta, S.; Bailey, L.J.; Benner, S.A.; Piccirilli, J.A. Affinity maturation of a portable Fab-RNA module for chaperone-assisted RNA crystallography. *Nucleic Acids Res.* **2018**, *46*, 2624–2635. [[CrossRef](#)]
- Sherman, E.; Archer, J.; Ye, J.D. Fab Chaperone-Assisted RNA Crystallography (Fab CARC). *Methods Mol. Biol.* **2016**, *1320*, 77–109. [[CrossRef](#)]
- Ye, J.D.; Tereshko, V.; Frederiksen, J.K.; Koide, A.; Fellouse, F.A.; Sidhu, S.S.; Koide, S.; Kossiakoff, A.A.; Piccirilli, J.A. Synthetic antibodies for specific recognition and crystallization of structured RNA. *Proc. Natl. Acad. Sci. USA* **2008**, *105*, 82–87. [[CrossRef](#)]

18. Koldobskaya, Y.; Duguid, E.M.; Shechner, D.M.; Suslov, N.B.; Ye, J.; Sidhu, S.S.; Bartel, D.P.; Koide, S.; Kossiakoff, A.A.; Piccirilli, J.A. A portable RNA sequence whose recognition by a synthetic antibody facilitates structural determination. *Nat. Struct. Mol. Biol.* **2011**, *18*, 100–106. [\[CrossRef\]](#)
19. Zhang, J.; Ferré-D'Amaré, A.R. Dramatic improvement of crystals of large RNAs by cation replacement and dehydration. *Structure* **2014**, *22*, 1363–1371. [\[CrossRef\]](#)
20. Zhang, J.; Ferré-D'Amaré, A.R. Post-crystallization Improvement of RNA Crystal Diffraction Quality. *Methods Mol. Biol.* **2015**, *1316*, 13–24. [\[CrossRef\]](#)
21. Stura, E.A.; Taussig, M.J.; Sutton, B.J.; Duquerroy, S.; Bressanelli, S.; Minson, A.C.; Rey, F.A. Scaffolds for protein crystallisation. *Acta Crystallogr. Sect. D* **2002**, *58*, 1715–1721. [\[CrossRef\]](#) [\[PubMed\]](#)
22. Center, R.J.; Kobe, B.; Wilson, K.A.; Teh, T.; Howlett, G.J.; Kemp, B.E.; Pountourios, P. Crystallization of a trimeric human T cell leukemia virus type 1 gp21 ectodomain fragment as a chimera with maltose-binding protein. *Protein Sci. A Publ. Protein Soc.* **1998**, *7*, 1612–1619. [\[CrossRef\]](#) [\[PubMed\]](#)
23. Ke, A.; Wolberger, C. Insights into binding cooperativity of MATa1/MAT α 2 from the crystal structure of a MATa1 homeodomain-maltose binding protein chimera. *Protein Sci. A Publ. Protein Soc.* **2003**, *12*, 306–312. [\[CrossRef\]](#)
24. Thorsen, T.S.; Matt, R.; Weis, W.I.; Kobilka, B. Modified T4 lysozyme fusion proteins facilitate G Protein-coupled receptor crystallogenesis. *Structure* **2014**, *22*, 1657–1664. [\[CrossRef\]](#) [\[PubMed\]](#)
25. Kim, S.H.; Quigley, G.J.; Suddath, F.L.; McPherson, A.; Sneden, D.; Kim, J.J.; Weinzierl, J.; Rich, A. Three-Dimensional Structure of Yeast Phenylalanine Transfer RNA: Folding of the Polynucleotide Chain. *Science* **1973**, *179*, 285. [\[CrossRef\]](#)
26. Francklyn Christopher, S.; Minajigi, A. tRNA as an active chemical scaffold for diverse chemical transformations. *FEBS Lett.* **2009**, *584*, 366–375. [\[CrossRef\]](#)
27. Ho, P.Y.; Yu, A.-M. Bioengineering of noncoding RNAs for research agents and therapeutics. *Wiley Interdiscip. Rev. RNA* **2016**, *7*, 186–197. [\[CrossRef\]](#)
28. Ponchon, L.; Dardel, F. Recombinant RNA technology: The tRNA scaffold. *Nat. Methods* **2007**, *4*, 571. [\[CrossRef\]](#)
29. Porter, E.B.; Polaski, J.T.; Morck, M.M.; Batey, R.T. Recurrent RNA motifs as scaffolds for genetically encodable small molecule biosensors. *Nat. Chem. Biol.* **2017**, *13*, 295–301. [\[CrossRef\]](#)
30. Cai, R.; Price, I.R.; Ding, F.; Wu, F.; Chen, T.; Zhang, Y.; Liu, G.; Jardine, P.J.; Lu, C.; Ke, A. ATP/ADP modulates gp16–pRNA conformational change in the Phi29 DNA packaging motor. *Nucleic Acids Res.* **2019**, *47*, 9818–9828. [\[CrossRef\]](#)
31. Lu, C.; Cai, R.; Grigg, J.C.; Ke, A. Using tRNA scaffold to assist RNA crystallization. In *RNA Scaffolds: Methods and Protocols, Methods in Molecular Biology*; Ponchon, L., Ed.; Springer: New York, NY, USA, 2021; Volume 2323, pp. 39–47.
32. Grigg, J.C.; Ke, A. Structural determinants for geometry and information decoding of tRNA by T box leader RNA. *Structure* **2013**, *21*, 2025–2032. [\[CrossRef\]](#) [\[PubMed\]](#)
33. Zuker, M. Mfold web server for nucleic acid folding and hybridization prediction. *Nucleic Acids Res.* **2003**, *31*, 3406–3415. [\[CrossRef\]](#) [\[PubMed\]](#)
34. Kao, C.; Zheng, M.; Rüdisser, S. A simple and efficient method to reduce nontemplated nucleotide addition at the 3 terminus of RNAs transcribed by T7 RNA polymerase. *RNA* **1999**, *5*, 1268–1272. [\[CrossRef\]](#) [\[PubMed\]](#)
35. Kabsch, W. XDS. *Acta Crystallogr. Sect. D Biol. Crystallogr.* **2010**, *66*, 125–132. [\[CrossRef\]](#) [\[PubMed\]](#)
36. Evans, P. Scaling and assessment of data quality. *Acta Crystallogr. Sect. D* **2006**, *62*, 72–82. [\[CrossRef\]](#)
37. McCoy, A.J.; Grosse-Kunstleve, R.W.; Adams, P.D.; Winn, M.D.; Storoni, L.C.; Read, R.J. Phaser crystallographic software. *J. Appl. Crystallogr.* **2007**, *40*, 658–674. [\[CrossRef\]](#)
38. Adams, P.D.; Afonine, P.V.; Bunkoczi, G.; Chen, V.B.; Davis, I.W.; Echols, N.; Headd, J.J.; Hung, L.-W.; Kapral, G.J.; Grosse-Kunstleve, R.W.; et al. PHENIX: A comprehensive Python-based system for macromolecular structure solution. *Acta Crystallogr. Sect. D* **2010**, *66*, 213–221. [\[CrossRef\]](#)
39. Emsley, P.; Lohkamp, B.; Scott, W.G.; Cowtan, K. Features and development of Coot. *Acta Crystallogr. Sect. D Biol. Crystallogr.* **2010**, *66*, 486–501. [\[CrossRef\]](#)
40. Keating, K.S.; Pyle, A.M. RCrane: Semi-automated RNA model building. *Acta Crystallogr. Sect. D Biol. Crystallogr.* **2012**, *68*, 985–995. [\[CrossRef\]](#)
41. Afonine, P.V.; Grosse-Kunstleve, R.W.; Echols, N.; Headd, J.J.; Moriarty, N.W.; Mustyakimov, M.; Terwilliger, T.C.; Urzhumtsev, A.; Zwart, P.H.; Adams, P.D. Towards automated crystallographic structure refinement with phenix.refine. *Acta Crystallogr. Sect. D* **2012**, *68*, 352–367. [\[CrossRef\]](#)
42. Chou, F.-C.; Sripakdeevong, P.; Dibrov, S.M.; Hermann, T.; Das, R. Correcting pervasive errors in RNA crystallography through enumerative structure prediction. *Nat. Methods* **2012**, *10*, 74. [\[CrossRef\]](#) [\[PubMed\]](#)
43. Green, N.J.; Grundy, F.J.; Henkin, T.M. The T box mechanism: tRNA as a regulatory molecule. *FEBS Lett.* **2010**, *584*, 318–324. [\[CrossRef\]](#) [\[PubMed\]](#)
44. Grundy, F.J.; Henkin, T.M. tRNA as a positive regulator of transcription antitermination in *B. subtilis*. *Cell* **1993**, *74*, 475–482. [\[CrossRef\]](#)
45. Suddala, K.C.; Zhang, J. High-affinity recognition of specific tRNAs by an mRNA anticodon-binding groove. *Nat. Struct. Mol. Biol.* **2019**, *26*, 1114–1122. [\[CrossRef\]](#) [\[PubMed\]](#)

46. Li, S.; Su, Z.; Lehmann, J.; Stamatopoulou, V.; Giarimoglou, N.; Henderson, F.E.; Fan, L.; Pintilie, G.D.; Zhang, K.; Chen, M.; et al. Structural basis of amino acid surveillance by higher-order tRNA-mRNA interactions. *Nat. Struct. Mol. Biol.* **2019**, *26*, 1094–1105. [[CrossRef](#)] [[PubMed](#)]
47. Battaglia, R.A.; Grigg, J.C.; Ke, A. Structural basis for tRNA decoding and aminoacylation sensing by T-box riboregulators. *Nat. Struct. Mol. Biol.* **2019**, *26*, 1106–1113. [[CrossRef](#)] [[PubMed](#)]
48. Zhang, J. Unboxing the T-box riboswitches—A glimpse into multivalent and multimodal RNA-RNA interactions. *Wiley Interdiscip. Rev. RNA* **2020**, *11*, e1600. [[CrossRef](#)]
49. Grigg, J.C.; Chen, Y.; Grundy, F.J.; Henkin, T.M.; Pollack, L.; Ke, A. T box RNA decodes both the information content and geometry of tRNA to affect gene expression. *Proc. Natl. Acad. Sci. USA* **2013**, *110*, 7240–7245. [[CrossRef](#)]
50. Wang, J.; Henkin, T.M.; Nikonowicz, E.P. NMR structure and dynamics of the Specifier Loop domain from the *Bacillus subtilis* tyrS T box leader RNA. *Nucleic Acids Res.* **2010**, *38*, 3388–3398. [[CrossRef](#)]
51. Wang, J.; Nikonowicz, E.P. Solution structure of the K-turn and Specifier Loop domains from the *Bacillus subtilis* tyrS T-box leader RNA. *J. Mol. Biol.* **2011**, *408*, 99–117. [[CrossRef](#)]
52. Grundy, F.J.; Winkler, W.C.; Henkin, T.M. tRNA-mediated transcription antitermination in vitro: Codon–anticodon pairing independent of the ribosome. *Proc. Natl. Acad. Sci. USA* **2002**, *99*, 11121–11126. [[CrossRef](#)] [[PubMed](#)]
53. Yousef, M.R.; Grundy, F.J.; Henkin, T.M. Structural Transitions Induced by the Interaction between tRNA^{Gly} and the *Bacillus subtilis* glyQS T Box Leader RNA. *J. Mol. Biol.* **2005**, *349*, 273–287. [[CrossRef](#)] [[PubMed](#)]
54. Vitreschak, A.G.; Mironov, A.A.; Lyubetsky, V.A.; Gelfand, M.S. Comparative genomic analysis of T-box regulatory systems in bacteria. *RNA* **2008**, *14*, 717–735. [[CrossRef](#)] [[PubMed](#)]
55. Gerdeman, M.S.; Henkin, T.M.; Hines, J.V. Solution structure of the *Bacillus subtilis* T-box antiterminator RNA: Seven nucleotide bulge characterized by stacking and flexibility. *J. Mol. Biol.* **2003**, *326*, 189–201. [[CrossRef](#)]
56. Suddala, K.C.; Cabello-Villegas, J.; Michnicka, M.; Marshall, C.; Nikonowicz, E.P.; Walter, N.G. Hierarchical mechanism of amino acid sensing by the T-box riboswitch. *Nat. Commun.* **2018**, *9*, 1896. [[CrossRef](#)]
57. Fang, X.; Michnicka, M.; Zhang, Y.; Wang, Y.X.; Nikonowicz, E.P. Capture and Release of tRNA by the T-Loop Receptor in the Function of the T-Box Riboswitch. *Biochemistry* **2017**, *56*, 3549–3558. [[CrossRef](#)]
58. Chetnani, B.; Mondragon, A. Molecular envelope and atomic model of an anti-terminated glyQS T-box regulator in complex with tRNA^{Gly}. *Nucleic Acids Res.* **2017**, *45*, 8079–8090. [[CrossRef](#)]
59. Grigg, J.C.; Ke, A. Sequence, structure, and stacking: Specifics of tRNA anchoring to the T box riboswitch. *RNA Biol.* **2013**, *10*, 1761–1764. [[CrossRef](#)]
60. Lehmann, J.; Jossinet, F.; Gautheret, D. A universal RNA structural motif docking the elbow of tRNA in the ribosome, RNase P and T-box leaders. *Nucleic Acids Res.* **2013**, *41*, 5494–5502. [[CrossRef](#)]
61. Zhang, J.; Ferré-D'Amaré, A.R. Direct evaluation of tRNA aminoacylation status by the T-box riboswitch using tRNA-mRNA stacking and steric readout. *Mol. Cell* **2014**, *55*, 148–155. [[CrossRef](#)]
62. Fauzi, H.; Agyeman, A.; Hines, J.V. T box transcription antitermination riboswitch: Influence of nucleotide sequence and orientation on tRNA binding by the antiterminator element. *Biochim. Biophys. Acta* **2009**, *1789*, 185–191. [[CrossRef](#)] [[PubMed](#)]
63. Gerdeman, M.S.; Henkin, T.M.; Hines, J.V. In vitro structure-function studies of the *Bacillus subtilis* tyrS mRNA antiterminator: Evidence for factor-independent tRNA acceptor stem binding specificity. *Nucleic Acids Res.* **2002**, *30*, 1065–1072. [[CrossRef](#)] [[PubMed](#)]
64. Grundy, F.J.; Rollins, S.M.; Henkin, T.M. Interaction between the acceptor end of tRNA and the T box stimulates antitermination in the *Bacillus subtilis* tyrS gene: A new role for the discriminator base. *J. Bacteriol.* **1994**, *176*, 4518–4526. [[CrossRef](#)] [[PubMed](#)]
65. Yousef, M.R.; Grundy, F.J.; Henkin, T.M. tRNA requirements for glyQS antitermination: A new twist on tRNA. *RNA* **2003**, *9*, 1148–1156. [[CrossRef](#)]
66. Giegé, R. Toward a more complete view of tRNA biology. *Nat. Struct. Mol. Biol.* **2008**, *15*, 1007. [[CrossRef](#)]
67. Maizels, N.; Weiner, A.M. Phylogeny from function: Evidence from the molecular fossil record that tRNA originated in replication, not translation. *Proc. Natl. Acad. Sci. USA* **1994**, *91*, 6729–6734. [[CrossRef](#)]
68. Pütz, J.; Giegé, R.; Florentz, C. Diversity and similarity in the tRNA world: Overall view and case study on malaria-related tRNAs. *FEBS Lett.* **2010**, *584*, 350–358. [[CrossRef](#)]
69. Gutmann, S.; Haebel, P.W.; Metzinger, L.; Sutter, M.; Felden, B.; Ban, N. Crystal structure of the transfer-RNA domain of transfer-messenger RNA in complex with SmpB. *Nature* **2003**, *424*, 699. [[CrossRef](#)]
70. Colussi, T.M.; Costantino, D.A.; Hammond, J.A.; Ruehle, G.M.; Nix, J.C.; Kieft, J.S. The structural basis of tRNA mimicry and conformational plasticity by a viral RNA. *Nature* **2014**, *511*, 366–369. [[CrossRef](#)]
71. Wang, W.; Chen, X.; Wolin, S.L.; Xiong, Y. Structural basis for transfer RNA mimicry by a bacterial Y RNA. *Structure* **2018**, *26*, 1635–1644. [[CrossRef](#)]
72. Reiter, N.J.; Osterman, A.; Torres-Larios, A.; Swinger, K.K.; Pan, T.; Mondragón, A. Structure of a bacterial ribonuclease P holoenzyme in complex with tRNA. *Nature* **2010**, *468*, 784–789. [[CrossRef](#)] [[PubMed](#)]
73. Zhang, J.; Ferré-D'Amaré, A.R. A flexible, scalable method for preparation of homogeneous aminoacylated tRNAs. *Methods Enzymol.* **2014**, *549*, 105–113. [[CrossRef](#)] [[PubMed](#)]

-
74. Bashan, A.; Agmon, I.; Zarivach, R.; Schlutzen, F.; Harms, J.; Berisio, R.; Bartels, H.; Franceschi, F.; Auerbach, T.; Hansen, H.A.S.; et al. Structural Basis of the Ribosomal Machinery for Peptide Bond Formation, Translocation, and Nascent Chain Progression. *Mol. Cell* **2003**, *11*, 91–102. [[CrossRef](#)]
 75. Schmeing, T.M.; Moore, P.B.; Steitz, T.A. Structures of deacylated tRNA mimics bound to the E site of the large ribosomal subunit. *RNA* **2003**, *9*, 1345–1352. [[CrossRef](#)] [[PubMed](#)]
 76. Hansen, J.L.; Schmeing, T.M.; Moore, P.B.; Steitz, T.A. Structural insights into peptide bond formation. *Proc. Natl. Acad. Sci. USA* **2002**, *99*, 11670. [[CrossRef](#)]
 77. Morais, M.C.; Koti, J.S.; Bowman, V.D.; Reyes-Aldrete, E.; Anderson, D.L.; Rossmann, M.G. Defining Molecular and Domain Boundaries in the Bacteriophage ϕ 29 DNA Packaging Motor. *Structure* **2008**, *16*, 1267–1274. [[CrossRef](#)]
 78. Ding, F.; Lu, C.; Zhao, W.; Rajashankar, K.R.; Anderson, D.L.; Jardine, P.J.; Grimes, S.; Ke, A. Structure and assembly of the essential RNA ring component of a viral DNA packaging motor. *Proc. Natl. Acad. Sci. USA* **2011**, *108*, 7357. [[CrossRef](#)]
 79. Byrne, R.T.; Konevega, A.L.; Rodnina, M.V.; Antson, A.A. The crystal structure of unmodified tRNA(Phe) from *Escherichia coli*. *Nucleic Acids Res.* **2010**, *38*, 4154–4162. [[CrossRef](#)]
 80. Moras, D.; Bergdoll, M. Packing and molecular interactions in tRNA crystals. *J. Cryst. Growth* **1988**, *90*, 283–294. [[CrossRef](#)]